Effect of El Niño–Southern Oscillation on the dynamical, thermal, and chemical structure of the middle atmosphere

F. Sassi, D. Kinnison, B. A. Boville, R. R. Garcia, and R. Roble
National Center for Atmospheric Research, Boulder, Colorado, USA

Received 9 December 2003; revised 21 June 2004; accepted 6 July 2004; published 14 September 2004.

[1] A simulation of the middle atmosphere is presented using a general circulation model (GCM) forced with observed sea surface temperature for the period 1950–2000. The GCM extends to the lower thermosphere and reproduces realistic dynamical and temperature distributions. The period contains several El Niño and La Niña events, which are identified using the NINO3 index. Composite anomalies of relevant meteorological fields are obtained by stratifying the northern winter season according to the NINO3 index. These anomalies have the structure of vertically propagating planetary waves extending from the troposphere to the mesosphere. Circulation anomalies in the middle atmosphere are accompanied by large temperature anomalies that are of opposite sign in the stratosphere and mesosphere, the former being warmer and the latter colder during El Niño events. Near the summer mesopause, changes in momentum deposition by parameterized gravity waves results in warming during El Niño. Detailed statistical analysis is used to determine the significance of these anomalies. A chemical/transport simulation is carried out using output from the GCM. It shows that when the lower stratosphere is colder (as during La Niña events), some ozone depletion takes place. Conversely, when the lower stratosphere is warmer and more disturbed, as is the case during El Niño events, heterogeneous chemical processes are inhibited. *INDEX TERMS:* 0340 Atmospheric Composition and Structure: Middle atmosphere—composition and chemistry; 3334 Meteorology and Atmospheric Dynamics: Middle atmosphere dynamics (0341, 0342); 3362 Meteorology and Atmospheric Dynamics: Stratosphere/troposphere interactions; *KEYWORDS:* middle atmosphere, ENSO, middle atmosphere structure and composition, time-dependent sea surface temperature, middle atmosphere variability

Citation: Sassi, F., D. Kinnison, B. A. Boville, R. R. Garcia, and R. Roble (2004), Effect of El Niño–Southern Oscillation on the dynamical, thermal, and chemical structure of the middle atmosphere, *J. Geophys. Res.*, *109*, D17108, doi:10.1029/2003JD004434.

1. Introduction

[2] Variability of the middle atmosphere reflects either anomalous boundary forcing or natural internal variations. Natural internal variability originates from nonlinearity of the stratospheric circulation [*Holton and Mass*, 1976; *Scott and Haynes*, 1998]. Boundary forcing results from vertically propagating wave disturbances (both at planetary scales, where Rossby waves are prominent, and at small scales, where gravity waves are more pronounced) and follows from variations of the tropospheric circulation [e.g., *Matsuno*, 1971; *Holton*, 1982]. The character of the stratospheric response depends critically on the magnitude of the tropospheric forcing [*Taguchi et al.*, 2001]. Additionally, forcing associated with perturbation of the radiative budget (such as those accompanying changes of composition of radiatively active constituents) can result in changes of the circulation and thermal structure.

0148-0227/04/2003JD004434$09.00

[3] Among a multitude of factors that can set up anomalous boundary forcing is a redistribution of tropical heat sources in the troposphere. In fact, during opposite phases of the El Niño–Southern Oscillation (ENSO) phenomenon (typically identified by its extreme events, El Niño and La Niña) anomalous wave trains propagate poleward in the winter hemisphere of the troposphere [*Horel and Wallace*, 1981; *Blackmon et al.*, 1983]. These wave trains are composed of a rich spectrum of zonal wave numbers [*Salby and Garcia*, 1987], one of whose manifestations in the troposphere is the well-known Pacific–North Atlantic (PNA) pattern. Present in those wave trains are planetary-scale waves that are able to propagate vertically into the stratosphere [*Garcia and Salby*, 1987], where they affect the structure of the wintertime polar vortex [*van Loon and Labitzke*, 1987].

[4] Evidence from models and observations points to a coupling between the troposphere and the middle atmosphere via anomalous propagation of planetary waves. For example, the polar vortex over northern Canada is shallower during El Niño events and the circumpolar vortex in the

lower stratosphere is weakened to the point that it can break up, leading to horizontal flow over the pole and to polar regions that are warmer than average [*van Loon and Labitzke*, 1987; *Hamilton*, 1993]. On the other hand, during La Niña events the vortex is well isolated and strongly zonally symmetric, and polar regions are somewhat colder than average. Not only is transport of constituents affected by these disturbances [*Leovy et al.*, 1985], but temperature-sensitive chemistry is also affected during extreme events [*Austin et al.*, 1992; *Shindell et al.*, 1998]. This is particularly important for ozone, a prominent radiatively active constituent whose variability feeds back onto the circulation and thermal structure.

[5] Attempts to isolate the ENSO effect from other elements of natural variability in the middle atmosphere have produced inconclusive results [*Hamilton*, 1993; *Baldwin and O'Sullivan*, 1995]. The difficulty of isolating ENSO effects in observations probably stems from the fact that variability associated with ENSO is not large compared to other natural factors. However, in a numerical model wherein ENSO is the only specified source of variability, it may be possible to isolate the ENSO signal in the middle atmosphere. To this end, we have used the Whole Atmosphere Community Climate Model (WACCM), a GCM developed at the National Center for Atmospheric Research. This model extends from the ground to the lower thermosphere and is forced with time-dependent sea surface temperature (SST) for the period 1950–2000. Because WACCM does not have a QBO, and does not include interactive chemistry, or radiative forcing from volcanic aerosols, the only sources of variability in the middle atmosphere are those associated with internal model dynamics and with the specified SST.

[6] Following a description of the model in section 2, section 3 illustrates the mean climate produced by the model during boreal winter (December–January–February). In section 4, we examine the dynamical and thermodynamical anomalies when Northern Hemisphere winters are partitioned based on the ENSO phase as indicated by the NINO3 index: We show that the model dynamics displays a characteristic signature, with opposite-signed response in the stratosphere and mesosphere. We examine the statistical significance of these anomalies in section 5. Section 6 deals with the implications of ENSO events for chemical composition of the middle atmosphere. Summary and conclusions follow in section 7.

2. Model Description

[7] WACCM1 is based on the National Center for Atmospheric Research's Community Climate Model Version 3 (CCM3) [*Kiehl et al.*, 1998a]. WACCM is run with 66 vertical levels from the surface to about 140 km. Vertical resolution is $\leq$1.5 km below 25 km. Above that altitude, vertical resolution decreases slowly to 2 km at the stratopause and 3.5 km in mesosphere; beyond the mesopause, the vertical resolution is one-half the local scale height. The horizontal resolution is T63, with 128 $\times$ 64 points in a quasi-linear grid [*Williamson*, 1997]. The dynamical equations are solved using a semi-Lagrangian technique [*Williamson and Olson*, 1994] with a time step of 1800 s.

[8] The climate produced by the standard 18-level of CCM3 version is discussed by *Hack et al.* [1998], *Hurrell et al.* [1998], and *Kiehl et al.* [1998b]. Although CCM3 produces a fairly realistic climate in the lower atmosphere, for simulations extending above the stratosphere the model needs to be complemented by additional physical processes appropriate to the upper atmosphere. Those processes include solar heating from absorption of radiation shortward of 200 nm, a spectrum of gravity waves launched at the tropopause, molecular viscosity, and ion drag. A detailed description of these physical parameterizations can be found by *Sassi et al.* [2002].

[9] The Model for Ozone and Related Chemical Tracers (MOZART) is a 3D global chemical transport model [*Brasseur et al.*, 1998; *Hauglustaine et al.*, 1998; *Horowitz et al.*, 2003]. The model horizontal and vertical resolution is determined by the input meteorological fields. MOZART is built on the framework of the Model of Atmospheric Transport and Chemistry (MATCH) [*Rasch et al.*, 1997].

[10] MOZART version 3 is used in this study. MOZART-3 was developed to represent chemical and physical processes from the surface to the middle atmosphere. This mechanism includes 48 chemical species and approximately 120 chemical and photochemical reactions. The species included are members of the O_x, NO_x, HO_x, ClO_x, and BrO_x chemical families, along with CH_4 and its degradation products. Nonmethane hydrocarbons are not included in this mechanism. Boundary conditions for N_2O, CO_2, CFC-11, CFC-12, HCFC-22, CFC113, CH_3CCl_3, CCl_4, CH_3Cl, CH_3Br, H1211, H1301 are representative of the 1995 atmosphere. The surface latitude, longitude, and seasonal distribution of CH_4 are taken from a present day MOZART-2 simulation. The model accounts for surface emissions of NO_x and CO based on the emission inventories as described by *Horowitz et al.* [2003]. A source of NO_x from lightning is distributed according to the location of convective clouds, based on *Price et al.* [1997], with a "C-shaped" vertical profile following *Pickering et al.* [1998]. Aircraft emissions of NO_x and CO are included in the model, based on *Friedl* [1997]. Heterogenous processes on sulfate aerosols and polar stratospheric clouds (type 1a, 1b, and 2) are included following the approach of *Considine et al.* [2000].

3. Boreal Winter Climate

[11] WACCM1 was forced with observed SSTs for the period 1950–2000 (NCEP Reynolds SST data set, http://podaac.jpl.nasa.gov/reynolds). Three 51 year realizations, starting on 1 January 1950, have been carried out, each one started from different initial conditions. The simulated zonal mean climate for Northern Hemisphere winter (December–January–February mean, DJF) is shown in Figure 1 between the ground and 100 km. The eastward polar night jet (Figure 1a) tilts equatorward in the mesosphere and reaches its largest intensity ($\sim$60 m s^{-1}) in the upper stratosphere and lower mesosphere. A zero wind line around 75–80 km marks the reversal of the zonal mean circulation due to the westward source of momentum from a spectrum of parameterized gravity waves; in the summer hemisphere, the zero wind line is located about 10–15 km higher. The zero wind line and the equatorward tilt of the jet in the winter

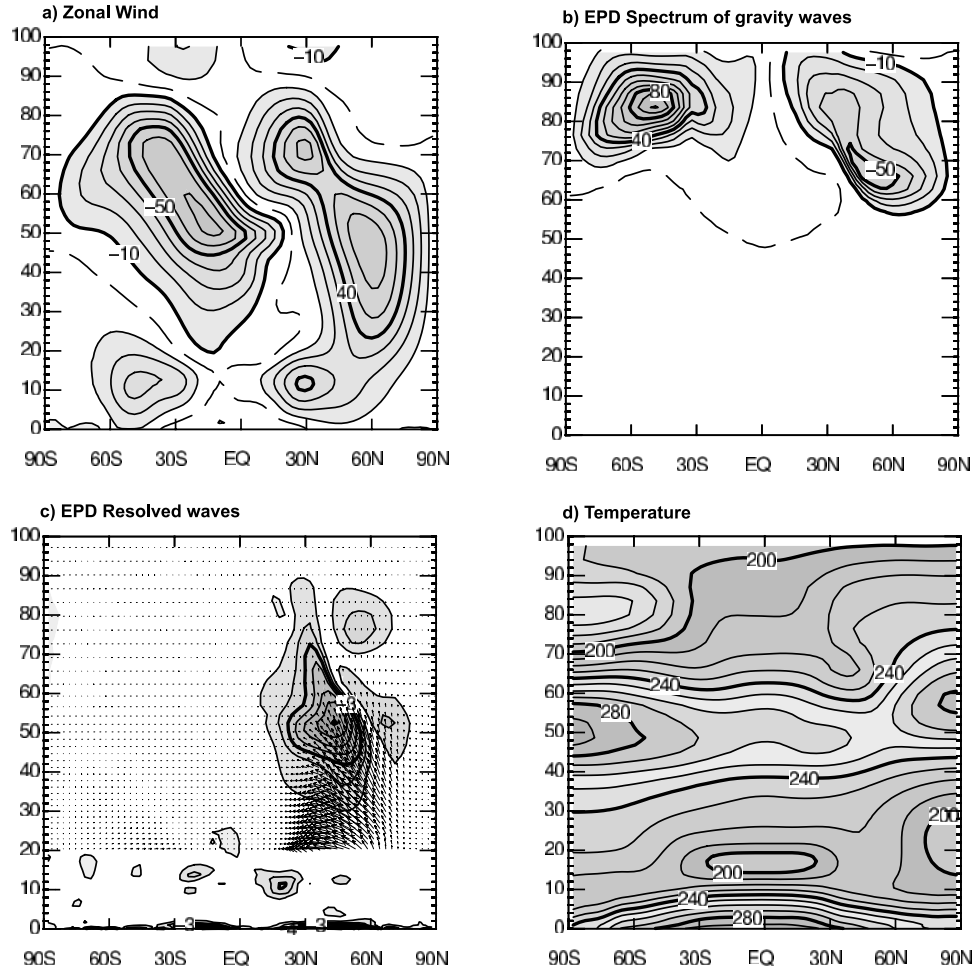

Figure 1. Time averages of December–January–February, averaged over the three simulations of (a) zonal mean zonal wind (m s^{-1}), (b) parameterized waves Eliassen-Palm flux divergence (EPD) (m s^{-1} day^{-1}), (c) resolved waves EPD (m s^{-1} day^{-1}), and (d) temperature (K). Contour intervals are 10 m s^{-1} in Figure 1a, 10 m s^{-1} day^{-1} in Figure 1b, 1 m s^{-1} day^{-1} in Figure 1c, and 10 K in Figure 1d.

hemisphere are realistic features of the zonal mean circulation in the mesosphere and lower thermosphere [e.g., *McLandress et al.*, 1996]; in the model, they are due solely to the momentum source from parameterized gravity waves (Figure 1b) [cf. *Sassi et al.*, 2002].

[12] This parameterized source of momentum is much larger than any contribution by resolved waves in the mesosphere. The largest accelerations ($\sim$100 m s^{-1} day^{-1}) due to the parameterized gravity waves are found in the summer hemisphere between 80 and 90 km, whereas somewhat smaller accelerations (~-50 m s^{-1} day^{-1}) are produced in the winter hemisphere some 10 km lower. Dissipation of resolved waves (Figure 1c), mostly planetary-scale Rossby waves, is prominent in the stratosphere, resulting in a source of westward zonal momentum peaking near the winter stratopause (~-4 m s^{-1} day^{-1}). Wave propagation in the meridional plane is illustrated by the vector field in Figure 1c, which is constructed from the meridional and vertical components of Eliassen-Palm Flux. Following a path that veers from the locations of largest zonal mean zonal wind, wave activity propagates upward and equatorward from the midlatitudes of the wintertime lower stratosphere.

[13] The combined resolved and parameterized sources of zonal momentum drive the summer-to-winter meridional circulation in the mesosphere, with upwelling in the summer hemisphere and downwelling at winter latitudes [*Dunkerton*, 1978; *Holton*, 1983]. Owing to the wave driving, the zonal mean temperature (Figure 1d) at the summer mesopause approaches 160 K, which is about 40 K colder than the winter mesopause. Although the model's summer mesopause is about 25 K warmer than in observations [*Lübken*, 2001], by and large the modeled thermal structure is realistic with a somewhat higher stratopause in winter than in summer and a realistic thermal structure in the lower stratosphere both at tropical and high latitudes.

[14] In order to illustrate the model's internal variability, Figure 2 shows the standard deviations (SD) of the time series of zonal mean temperature calculated for the months of December through March. Throughout winter, the SD of temperature shows two distinct regions of variability at high northern latitudes, with maxima approaching 10 K in the mesosphere and 6 K in the stratosphere. There are also significant intraseasonal variations of SD, particularly in the location of the largest values: The overall largest SD is calculated in February in the poleward flank of the mean

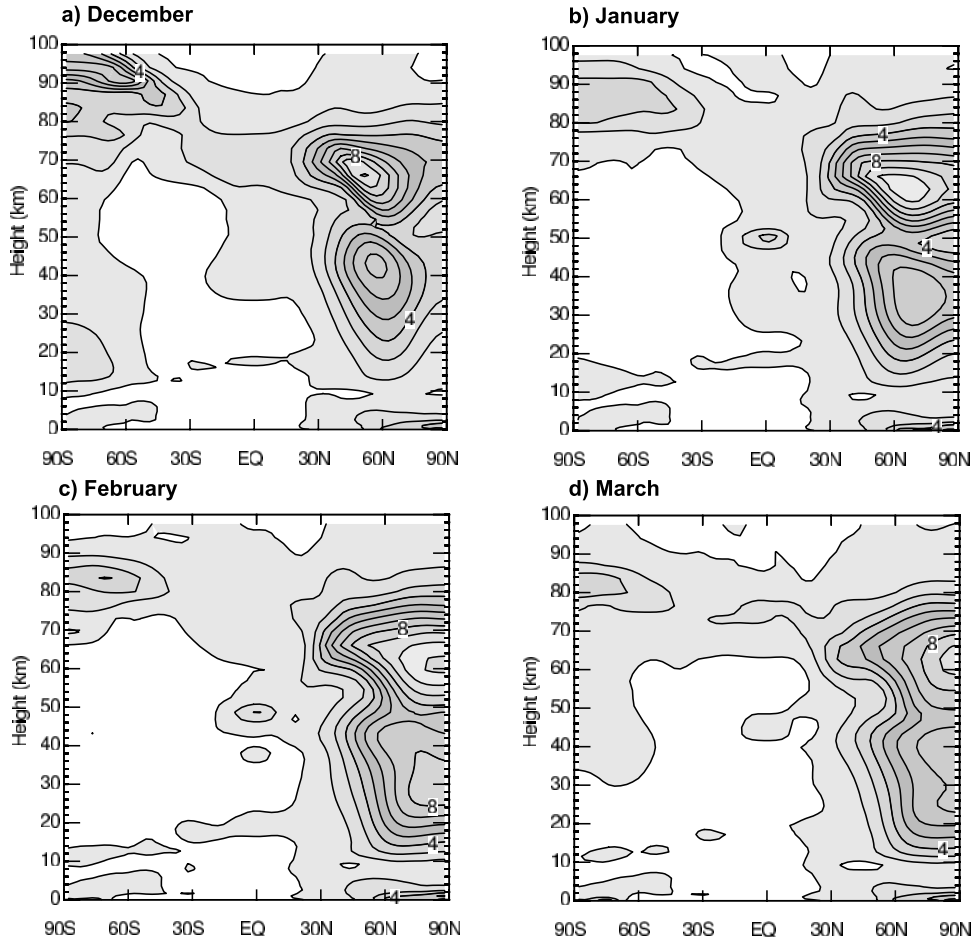

Figure 2. Standard deviation of temperature for the months of (a) December, (b) January, (c) February, and (d) March. Contour interval is 1 K in all panels.

eastward stratospheric jets (compare Figure 1a), but in January the largest SD is found near 60N, well inside the mean position of the jet core, similar to December but occupying a broader region. The weakest SD of temperature is realized in March. These differences underscore the variability of wave propagation and dissipation during northern winter and these results are consistent with other model simulations [e.g., *Hamilton*, 1995].

[15] Figure 2 shows considerable temperature variability near the summer mesopause, particularly during December. The variability results from variations in the forcing by the parameterized gravity waves (not shown). Because this feature depends on poorly known aspects of a parameterized process, and because observations are not available to verify it, we cannot determine unambiguously whether that summer mesopause variability produced by the model reflects observable features or is just an artifact of the parameterized spectrum of gravity waves. Nonetheless, we show below that in the model there is a statistically significant signal at the summer mesopause that is associated with ENSO variability.

4. Dynamical and Thermodynamical Anomalies Associated With ENSO

[16] A conventional way to characterize the state of the tropical Pacific Ocean at any given time is to calculate the corresponding NINO3 index, which measures the normalized standard deviation of SST in the eastern Pacific between 5S and 5N, and 150W and 90W. Time series of the corresponding NINO3 index for the months of December, January, February and March, from 1950 through 2000, are shown in Figure 3 (see figure caption for details). When the index exceeds +1 SD, that event is referred to as El Niño; when the index exceeds −1 SD, that event is called La Niña.

[17] Several maxima and minima exceeding ±1 SD (horizontal lines in Figure 3) are seen during the period 1950–2000, but only those that persist throughout DJF (at least 2 months during winter must exceed the ±1 SD threshold) are denoted by blue (La Niña) and red (El Niño) arrows in Figure 3. They are also listed in Table 1, which shows that 9 El Niño and 11 La Niña events are identified in this record. The most positive excursions occur during El Niño events of the mid-1980s and late 1990s; the most negative excursions occur during La Niña events of the 1950s, 1970s, and late 1980s. In particular the period from the late 1980s to the early 1990s is characterized by a fairly rapid transition from La Niña conditions to more frequent El Niños (compare Table 1). The period between 1988 and 1993 (indicated by the two vertical dashed lines in Figure 3) is examined specifically regarding the chemical response to ENSO in section 6.

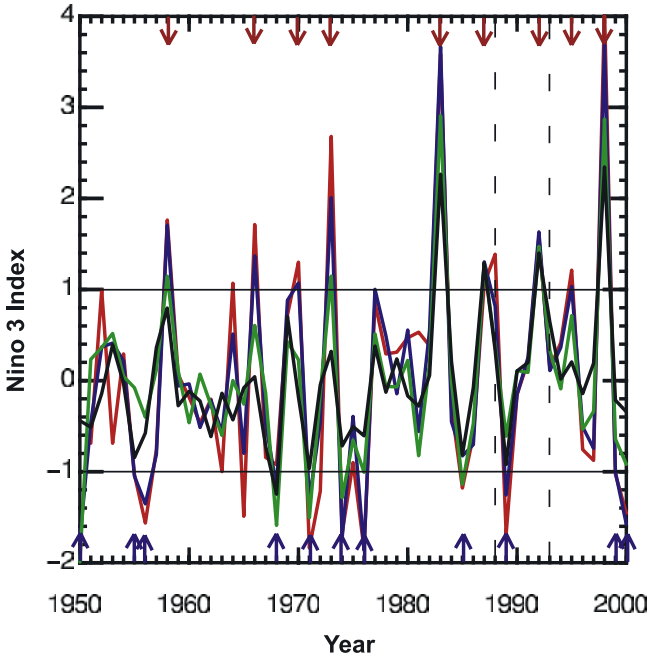

Figure 3. Time series of NINO3 index of every December (red), January (blue), February (green), and March (black) in the 1950–2000 sea surface temperature (SST) data set. Red arrows at the top indicate the major El Niño events, while the blue arrows at the bottom indicate the major La Niña events. The vertical dashed line indicates the time period of the Model for Ozone and Related chemical Tracers (MOZART) simulation. The horizontal solid lines show the threshold for extreme El Niño–Southern Oscillation (ENSO) events.

[18] From the ensembles of years in Table 1, composite differences El Niño minus La Niña are calculated during northern winter for each month. Composite differences for the zonal mean temperature are shown in Figure 4, from December throughout March. From the beginning throughout the middle of winter (Figures 4a and 4b), temperature anomalies are somewhat small. In fact they are almost nonexistent during January (Figure 4b), except in the tropical troposphere. On the other hand, the anomalies are substantial during late winter and early spring (Figures 4c and 4d). In particular during February, temperature anomalies are in excess of 7 K in the stratosphere and −6 K in the mesosphere. A quadrupole feature is seen in the middle atmosphere, with warm and cold anomalies juxtaposed at polar and subtropical latitudes. The high-latitude anomalies are considerably larger than those at low latitudes, reflecting the behavior of the global overturning circulation, which produces large vertical velocities in the polar regions. Note that the pattern of the temperature anomalies is such that during El Niño events the high-latitude stratosphere is generally warmer while the overlying mesosphere is colder. Note also the overall warming of about 1 K in the tropical troposphere, a well documented feature of the mature phase of El Niño events [e.g., *Yulaeva and Wallace*, 1994].

[19] We now examine the zonally asymmetric structures that accompany the zonal mean anomalies of Figure 4. Figure 5 illustrates the temperature anomaly during February at three elevations in the model. At 500 hPa (Figure 5a), anomalies (±3 K) extend from the Pacific Ocean to north America forming a wavetrain that is reminiscent of the PNA pattern [*Horel and Wallace*, 1981]. The PNA pattern is a salient feature of tropospheric dynamics, but it includes waves at zonal scales that do not extend very far in the middle atmosphere, where only the longest zonal scales can propagate [*Charney and Drazin*, 1961]. This is shown at 50 hPa (Figure 5b), where the temperature anomaly pattern reveals a prominent wave-1 component. Note that the positive temperature anomaly over northern Canada (9 K) is accompanied by a positive height anomaly (not shown), which is associated with a weaker polar night jet. At 3.3 hPa (Figure 5c), the temperature anomaly (13 K) is also dominated by a wave-1 structure, rotated westward with respect to the lower-stratospheric anomaly. This feature is indicative of the prominence of upward propagating planetary Rossby waves.

[20] It is worthwhile to compare the model anomalies to the model reanalysis. We have used data from the National Centers for Environmental Prediction and National Center for Atmospheric Research (NCEP/NCAR) reanalysis [*Kistler et al.*, 2001] for the period 1950 to 1999. Figure 6 shows temperature anomalies at 500 hPa and 50 hPa during February for the same El Niño minus La Niña composites used in Figure 5. The temperature anomaly at 500 hPa is remarkably similar to that in the model (Figure 5a), although the latter is more extensive, reaching around the globe.

[21] Figure 7a shows the anomalous Eliassen-Palm flux divergence (EPD) due to resolved waves averaged from December through March. Figure 7b shows the EPD anomaly due to parameterized gravity waves. Anomalous westward EPD from resolved waves (~ -2.5 m s^{-1} day^{-1}) is found in the upper stratosphere and lower mesosphere at winter midlatitudes. At the same time, an anomaly of eastward EPD (~ 6 m s^{-1} day^{-1}), generated by parameterized gravity waves, is shown in the winter mesosphere, and is mirrored in the summer hemisphere by an anomaly of opposite sign. Note that, while the anomaly of resolved EPD reinforces the time mean accelerations in the stratosphere (Figure 1c), the anomaly of parameterized EPD opposes the mean accelerations in the mesosphere (Figure 1b) in both hemispheres.

[22] It is worthwhile noting that, due to filtering by the stratospheric zonal winds, the anomalies in Figure 7 are not independent. Specifically, a negative (westward) EPD anomaly in the stratosphere results in a weaker eastward

Table 1. El Niño/La Niña Events

El Niño	La Niña
1957–1958	1949–1950
1965–1966	1954–1955
1969–1970	1955–1956
1972–1973	1967–1968
1982–1983	1970–1971
1986–1987	1973–1974
1991–1992	1975–1976
1994–1995	1984–1985
1997–1998	1988–1989
	1998–1999
	1999–2000

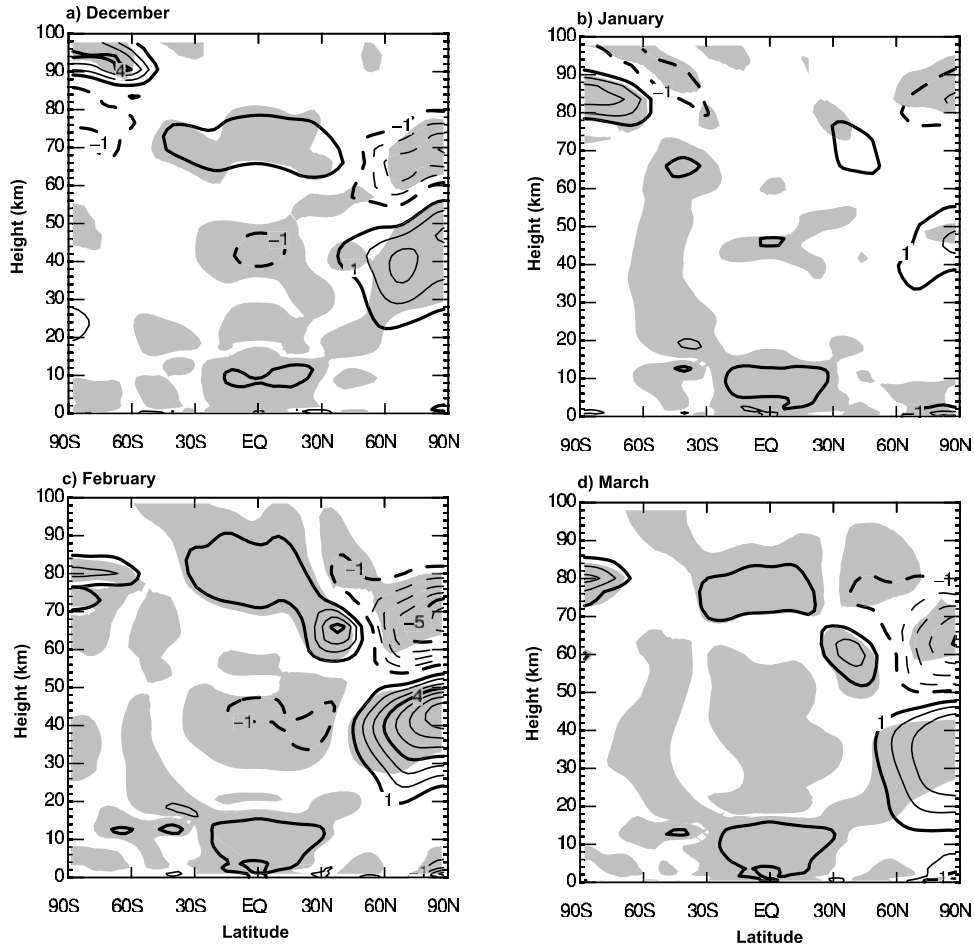

Figure 4. El Niño minus La Niña zonal mean temperature anomalies (K) during (a) December, (b) January, (c) February, and (d) March. Contour interval is 1 K. Shading indicates anomalies that are significant at least at a 95% level according to the Monte Carlo test.

polar night jet. This is accompanied by reduced filtering of eastward propagating gravity waves, and ultimately leads to an anomalous source of positive (eastward) momentum in the mesosphere.

5. Statistical Analysis

5.1. Monte Carlo Analysis

[23] The composite differences shown in section 4 illustrate the response of the middle atmosphere to extremes of the ENSO cycle (El Niño minus La Niña events). It remains to be shown that the magnitude of these anomalies is significant compared to the model's internal variability. Figure 2 shows that, over the ensemble of three 51 year simulations, the SD of temperature in the middle atmosphere has maxima of $\sim$7–10 K during northern winter. We show next that some of the composite differences of Figure 4, calculated from a sample of 27 El Niño and 33 La Niña events, are highly statistically significant, taking into account the smaller sample size of the composite differences.

[24] In order to verify the statistical significance of the ENSO-related anomalies, we carry out a Monte Carlo–type analysis by sampling randomly the 153 years(=51 years $\times$ 3 realizations) of model output into groups of 27 and 33 members, respectively. Differences between the two groups calculated 1000 times provide a mean expected value and a SD about the mean. The distribution of the differences is Gaussian with a mean value close to zero (not shown). For a normal distribution, 1.96 $\times$ SD represents a range of values about the mean having a 5% probability of occurring by chance; any value exceeding this range is thus significant beyond a 95% level of significance.

[25] The distribution of temperature differences exceeding the 95% confidence interval for the months of December, January, February and March is shown by the shaded areas in Figure 4. Compared to the composite differences (contours in Figure 4), February and March show anomalies that are statistically significant throughout the middle atmosphere. During December, the response in the stratosphere is still statistically significant, as are some locations in the northernmost latitudes of the mesosphere. As expected, the January anomalies, by and large, are not significant in the middle atmosphere. The tropospheric anomaly is statistically significant during every month of this analysis. Similar results are obtained by sampling of the zonal wind (not shown). The signal and its significance decrease in the lower stratosphere, and the net result is a lack of statistical significance of the zonal mean anomalies below about 30 km.

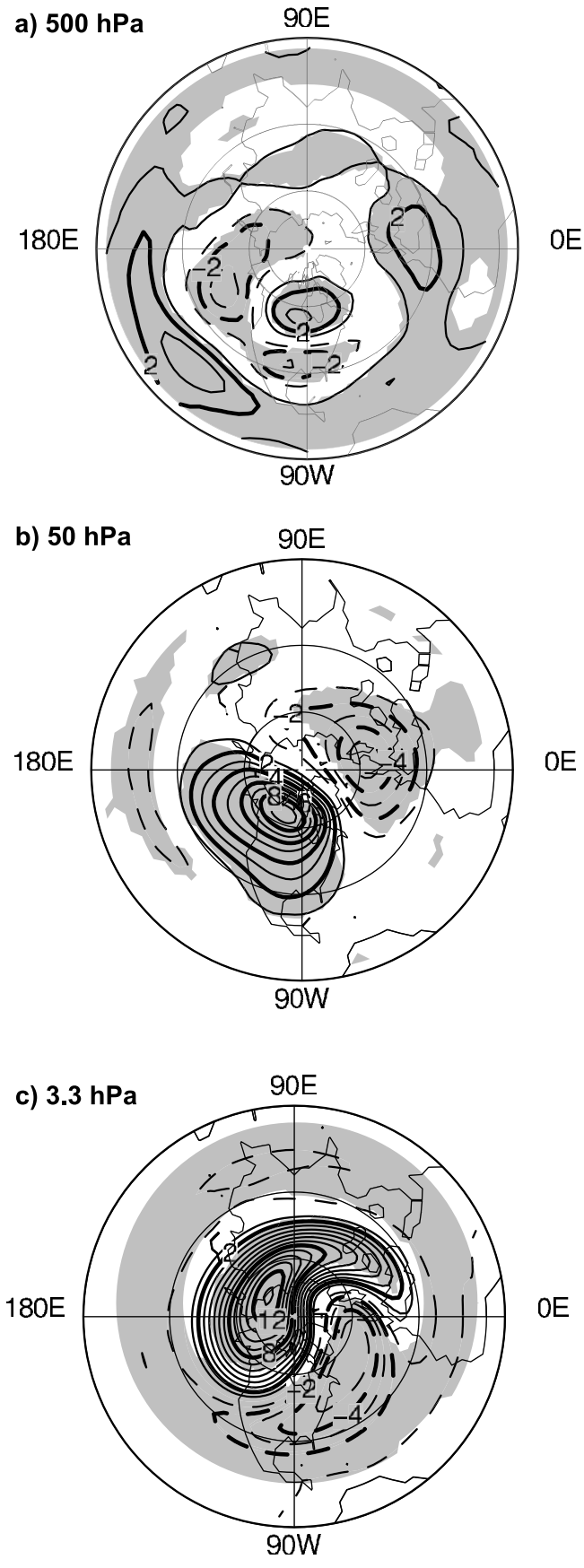

[26] The zonally asymmetric response to ENSO extremes displays larger anomalies than the zonal mean. The results of a Monte Carlo analysis in this case are shown as shaded areas in Figure 5 for temperature at 500, 50 and 3.3 hPa during the month of February. The patterns of the horizontal anomalies are statistically significant at all levels (Figures 5a–5c).

[27] The modeled changes in wave amplitudes (mostly in the form of planetary Rossby waves) between El Niño and La Niña events are statistically significant, even in the lower stratosphere. However, the effect on the zonal mean state is statistically significant only in the middle and upper stratosphere, and to a lesser extent in the mesosphere. At these higher altitudes the waves dissipate most strongly, and thus force changes in the zonal mean state.

5.2. Empirical Orthogonal Function (EOF) Analysis of the Zonal Mean Field

[28] We now investigate how much of the amplitude of middle atmosphere empirical orthogonal function (EOF) patterns in the latitude/height plane is associated with ENSO. The Monte Carlo analysis constitutes a local test of statistical significance, although the statistically significant regions form coherent patterns in the latitude/height plane. On the other hand, an EOF analysis reveals the leading spatial patterns of variability and their temporal evolution (principal components), both of which can be used for statistical inferences.

[29] Figure 8 shows the first EOF (EOF1) of zonal mean temperature for February. The EOFs of the other winter months (not shown) show similar patterns. The EOFs are calculated from monthly mean output: for each month the three 51 year simulations are concatenated to obtain a total record of 153 years, and the time mean is removed. The leading EOF (EOF1) explains 60% of the total variance and shows two distinct anomalies at middle to high latitudes of the winter hemisphere with opposing signs. Along with anomalies at subtropical latitudes with opposite signature, these features reflect anomalous downwelling/upwelling taking place in the polar middle atmosphere, and opposing vertical motions at low latitudes due to mass conservation. Higher EOFs explain much smaller fractions of the variance than EOF1 (usually less than 15%) and are not shown here.

[30] The patterns in Figure 8 are similar to the composite differences in Figure 4. It should be noted that the EOFs shown in Figure 8 reflect the climatological variability of the atmosphere, during winter, and that the atmospheric response during El Niño and La Niña events represents only a small fraction of that variability. EOF1 explains the largest percentage of middle atmosphere variance (~67%) in January (not shown).

[31] Associated with the spatial pattern of EOF1 is its temporal variation, or principal component (PC1). One can compute the linear correlation between PC1 and the NINO3 index in order to estimate what fraction of the variance of

Figure 5. El Niño minus La Niña polar projections of temperature at (a) 500 hPa, (b) 50 hPa, and (c) 3.3 hPa during February. Contour interval is 1 K in all panels. Shading indicates anomalies that are significant at least at a 95% level according to the Monte Carlo test.

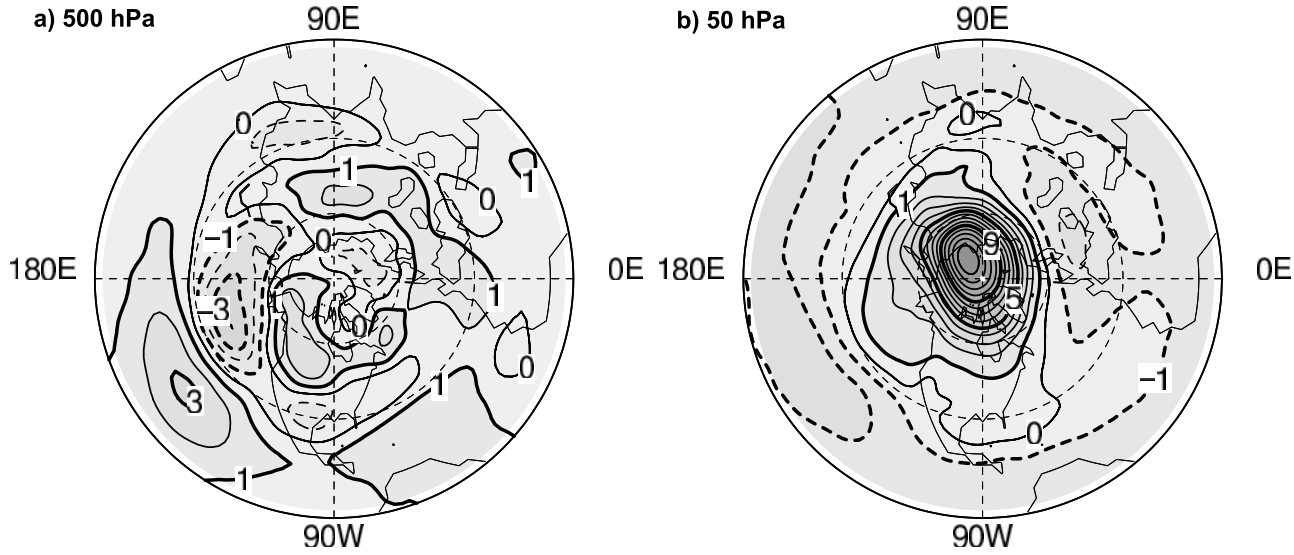

Figure 6. El Niño minus La Niña polar projections of the National Centers for Environmental Prediction and National Center for Atmospheric Research (NCEP/NCAR) reanalysis temperature using the same years that went into the composites of Figures 6, 7, and 8: (a) 500 hPa; (b) 50 hPa. Contour interval is 1 K in both panels.

PC1 can be attributed to ENSO. Figure 9 shows the temporal traces of PC1 and NINO3 for the month of February. In the figure, the values of PC1 for the three 51 year realizations are shown consecutively. The NINO3 index is repeated for each 51 year segment. The coefficient of linear correlation is 0.17, which barely exceeds the 95% confidence interval (~0.16) for time series with 153 degrees of freedom. While the coefficient is somewhat larger in March (0.22) and December (0.19), during January it is less than 0.1. The February linear correlation coefficient of 0.17 between NINO3 and PC1 indicates that the former explains only about 2.8% of the variance of PC1, or about 1.7% of the total variance of the original temperature time series (since 60% of the temperature variance is explained by EOF1).

[32] Closer inspection of Figure 9 shows that the largest local maxima of NINO3 correspond better to local maxima of PC1 (as in the early 1970s, 1980s and late 1990s) than the minima of NINO3 correspond to minima of PC1. This suggests that warm SST may exert a greater influence on the variability of the middle atmosphere than do cold SST. Indeed, a calculation using only those instances when the

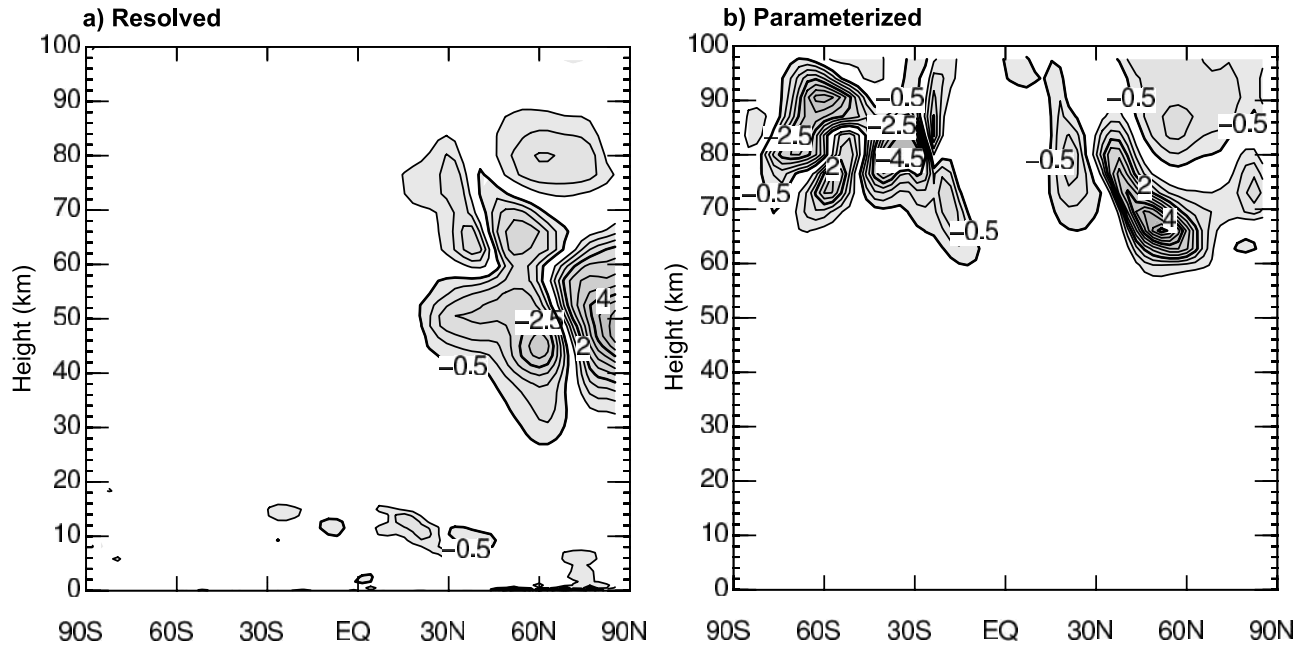

Figure 7. (a) The resolved waves' EPD and (b) the parameterized waves' EPD averaged from December throughout March. Contour interval is 0.5 m s^{-1} day^{-1} in both panels.

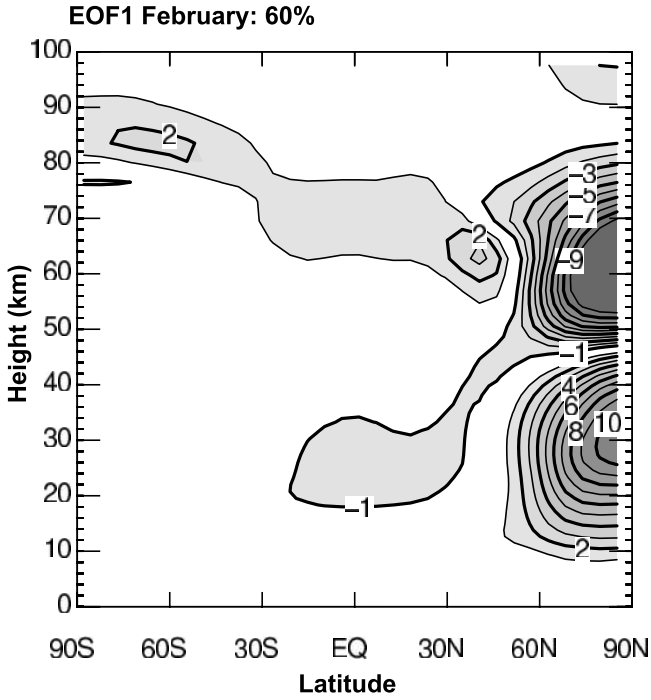

Figure 8. First empirical orthogonal function (EOF) mode of temperature obtained from concatenating the three realizations in one 153 year time series for February.

NINO3 index is positive yields a correlation coefficient with PC1 of 0.28 during February, which is above the 95% confidence interval (∼0.23) for time series with 75 degrees of freedom (25 × 3, where 25 is the number of instances where NINO3 is positive). A correlation coefficient of 0.28 implies that about 7.8% of the variance of EOF1, or 4.7% of the total variance of temperature, is explained in terms of positive variations of NINO3. We also computed the correlation between PC1 and NINO3 using only instances when the latter was negative. In this case, a much smaller correlation coefficient (about 0.1) is obtained, which is not statistically significant.

[33] Figure 10 shows the NINO3 index and PC1 of Figure 9 plotted against each other in a scatter diagram. The scatter diagram shows that there is a small but significant difference in the mean values of PC1 between the groups of La Niña and El Niño cases (indicated by the blue and red crosses, where the width of the arms denotes the standard error). Figure 10 also shows that, while El Niño cases are biased toward positive PC1, the ensemble of La Niña events is more or less uniformly distributed between positive and negative values of PC1. In this regard, the distribution and mean of La Niña events resembles those of the neutral events (whose mean is denoted by the black cross).

[34] Using a t-test, the means of the extreme events (El Niño vs. La Niña cases) are statistically different at about the 95% level, consistent with the Monte Carlo simulation of section 5.1. Similarly, the mean of the neutral events and of the combined neutral and La Niña events (green cross) are both distinguishable from the mean of El Niño events (at the 99% confidence level). The average of La Niña events, however, is not statistically distinguishable from the average of the neutral events. A similar result was obtained by *Hamilton* [1995] who showed that by imposing warm/cold tropical SST anomalies, the atmospheric response to the cold events is somewhat similar to the base, undisturbed case. This result indicates that the small correlation between NINO3 and PC1 found above arises almost entirely from extreme excursions of the NINO3 index. In fact, even when NINO3 > 1, its linear correlation with PC1 is small, so that NINO3 always explains less than 10% of the total variance of zonal mean temperature in the middle atmosphere. This implies that only a small fraction of the middle atmosphere variability in the model is driven by variations of tropical SST. In fact, even the effect of ENSO at midlatitudes of the troposphere does not exceed 30%, and is localized to the PNA region [*Saravanan*, 1998]. Globally, the effect of ENSO is likely to be much smaller even in troposphere.

6. Chemical Anomalies

[35] The dynamical response illustrated in the previous sections can drive chemical variability. Because WACCM1 does not include interactive chemistry, we have run the

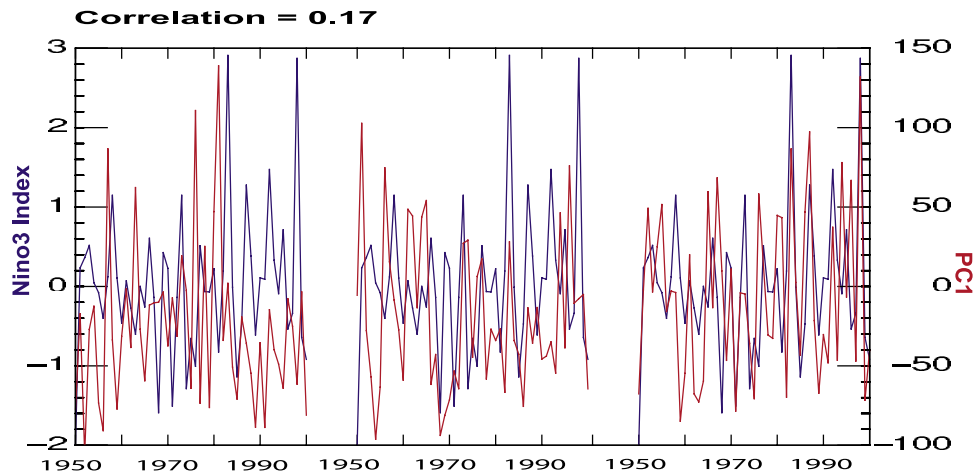

Figure 9. PC1 (red) corresponding to the February EOF1 in Figure 9, and NINO3 index (blue) repeated periodically at the end of each 51 year segment. The coefficient of linear correlation is 0.17.

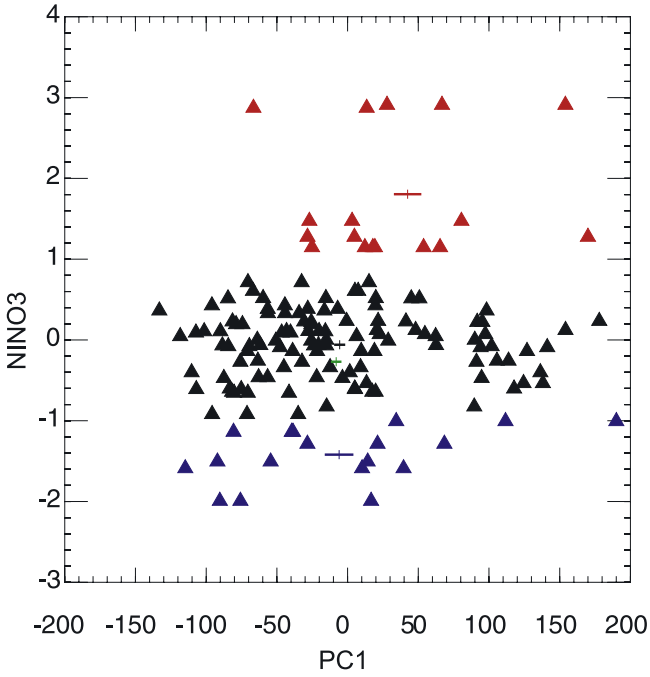

Figure 10. Scatter diagram of the PC1 and NINO3 of Figure 9. Red triangles show the El Niño events; blue triangles show the La Niña events; black triangles show the average years. The crosses show the average of each population (colored according to the triangles), with the extent of the horizontal arm of the cross indicating the standard deviation of the mean of each population. The green cross is the average of the neutral and La Niña events.

offline chemistry model, MOZART-3, using 3 hourly WACCM1 output from one realization of the period 1988 through 1992, which includes opposite extrema of ENSO.

[36] Figure 11 shows the temporal evolution of zonal mean temperature (Figure 11a), nitric acid (Figure 11b) which is relevant to ozone depletion, and ozone (Figure 11c) at 84N, between 200 hPa and 6 hPa, for the duration of the MOZART-3 simulation. Temperature is a good indicator of the state of the polar vortex during northern winter. The winter 1988–1989 (a strong La Niña year) is very cold, with temperatures reaching 186 K in the middle of northern winter. More importantly, cold temperatures persist through early spring (dotted vertical lines identify 1 April of each year), as indicated by the heavy contour in Figure 11a, which highlights the 194 K isotherm. The winter of 1989–1990 has warmer temperatures, but the vortex remains isolated through early spring. Temperatures in the middle of the following winter (1990–1991) are as cold as in 1988–1989, but they do not last through springtime. Finally, the winter of 1991–1992 (a strong El Niño year) is characterized by relatively warmer air during northern winter and a rapid breakup of the vortex in early spring.

[37] The dynamical signatures implied by temperature evolution affect stratospheric chemical composition via transport and photochemical effects. During the very cold and long winter of 1988–1989, significant denitrification takes place (denitrification occurs in the model when temperature is below 194 K), with concentrations of nitric acid falling below 3 ppbv from the middle of winter to early spring. At the same time, significant chlorine activation occurs in early spring (not shown). Note that both denitrification and chlorine activation are precursors of ozone depletion, as long as they persist through early spring. This is the case during winter 1988–1989, when substantial ozone depletion is simulated: ozone mixing ratios in the lower stratosphere decrease below 2 ppmv by 1 April. The winter of 1989–1990 shows some denitrification near the beginning of the year but because of the early breakup the vortex, ozone loss is curtailed. The following winter (1990–1991) has much colder temperatures, which give rise to substantial denitrification, but the early breakup of the vortex prevents extensive ozone loss. Finally, the winter of 1991–1992 is warmer and temperature rarely drops below 194 K; denitrification is suppressed, and minimal ozone loss is calculated.

7. Summary and Conclusions

[38] A general circulation model without interactive chemistry, a quasibiennial oscillation, or volcanic aerosols has been used to isolate the effects of ENSO on the structure and composition of the middle atmosphere. By imposing observed SST for the period 1950–2000, several major El Niño and La Niña events are reproduced in the simulation; these events are identified using the NINO3 index, a measure of sea surface temperature variability in eastern Pacific. Because of the present interest in chemical changes in the Artic polar vortex, the chemical response in the middle atmosphere has also been studied, with particular emphasis on northern winter and early spring.

[39] The model's mean climatology reveals that Rossby planetary waves affect the zonal mean circulation up to about the stratopause, but in the mesosphere parameterized gravity waves become increasingly important. A spectrum of parameterized gravity waves is imposed at 100 hPa and allowed to propagate through the stratospheric wind system, where it is subject to selective filtering depending on phase velocity. The spectrum of waves reaching the stratopause provides the largest source of momentum in the mesosphere.

[40] In winter the model displays a characteristic pattern of zonally averaged variability that reflects changes in the strength of the mean meridional circulation of the middle atmosphere. Largest temperature anomalies occur at high latitudes of the stratosphere and mesosphere; accompanying these thermal anomalies are wind anomalies that reflect the varying intensity of the polar night jet.

[41] By taking the difference between El Niño and La Niña events, we have extracted the variability associated with extreme occurrences of ENSO. We show that these composite differences have the same spatial pattern as the model's total variability, its amplitude reflecting a strengthening of the stratospheric mean meridional circulation and a weakening of its mesospheric counterpart during El Niño events. The magnitude of these effects is larger during late winter and early spring than in early and midwinter. The fact that the composite differences show the same overall pattern as the model's total variability is consistent with the fact that the latter is determined by a variety of forcing mechanisms (internal as well as external), of which variations in SST are just a special case.

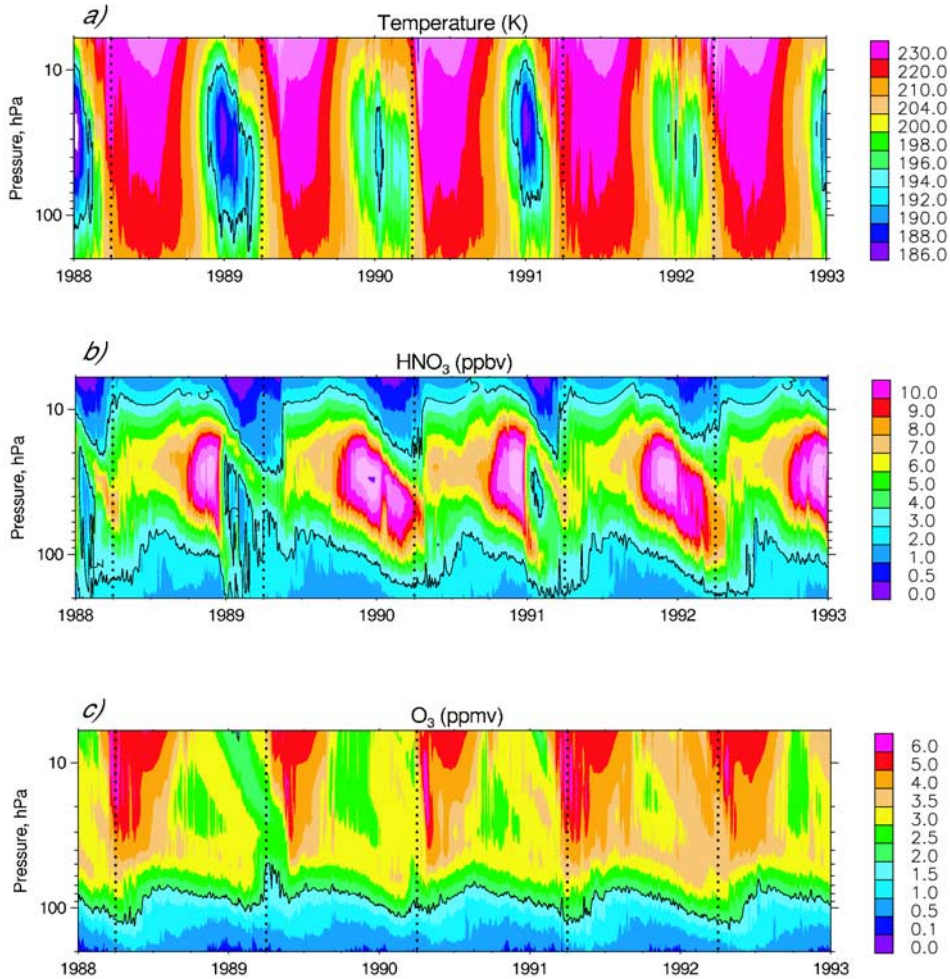

Figure 11. Time-height plot of the (a) zonal mean temperature and (b) zonal mean nitrous oxide at 84°N during the MOZART-3 simulation, 1988–1992. The vertical dotted line indicates 1 April of each year. The solid line in Figure 11a identifies the 194 K contour and in Figure 11b the 20 ppbv.

[42] Zonal wind anomalies are predominantly westward during El Niño events throughout the stratosphere and lower mesosphere in late winter and early spring; weakly westward in early winter, and lack a coherent pattern in midwinter. They are driven by planetary wave anomalies propagating upward from the lower stratosphere and dissipating in the upper stratosphere. The zonal wind anomalies also lead to anomalous filtering of parameterized gravity waves, which give rise to large of eastward momentum anomalies in the mesosphere during late winter and early spring. The momentum anomalies during El Niño events are consistent with a strengthening of the mean meridional circulation in the stratosphere, and a weaking of the same in the mesosphere. The calculated temperature anomalies then follow from the strengthening/weakening of the mean meridional circulation in the middle atmosphere.

[43] We have used two statistical methods to determine the significance of the calculated anomalies: A Monte Carlo calculation and an EOF analysis. The Monte Carlo calculations reveal that the zonally asymmetric anomalies are statistically significant throughout the middle atmosphere, even in the lower stratosphere. The zonal mean response is statistically significant in the middle atmosphere mainly in late winter and early spring, when the anomalies are the largest. Weak statistical significance is attained in early winter, and no significance in midwinter. It should be noted that while the zonal mean anomalies are significant mostly in the upper stratosphere and mesosphere (where wave dissipation is pronounced), the wave anomalies are significant at all levels.

[44] We also attempted to establish a relationship between middle atmosphere variability (represented by the principal component, PC1, of the leading EOF) and changes in SST (represented by the NINO3 index). The coefficient of linear correlation between PC1 and NINO3 barely exceeds the threshold of significance, and overall helps to explain less than 10% of the concurrent variations of the two time series. The EOF analysis also shows that, while there is a good correspondence between positive excursions of the NINO3 index and those of PC1, the reverse is not true for negative excursions. The latter, which correspond to La Niña events, do not behave differently from neutral years, i.e., those years in which the NINO3 index deviates from zero by less than 1 SD.

[45] Chemical anomalies follow from temperature changes, because of the dependence of heterogeneous chemistry on ambient temperature. Although lack of computational resources precluded long calculations of middle

atmosphere photochemistry, a simulation was carried out for the period 1988–1992, when SST swing from La Niña conditions in the late 1980s to the more persistent El Niño conditions of the early 1990s. During La Niña events, when the polar vortex tends to be more stable, colder, and persistent through early spring, conditions favor denitrification and chlorine activation. These, in turn, lead to ozone depletion in early spring. On the other hand, during El Niño events the vortex is strongly disturbed, polar air mixes readily with air from lower latitudes, and temperatures are relatively warm over the polar cap. Under these circumstances, ozone destruction is minimized.

[46] **Acknowledgment.** The National Center for Atmospheric Research is sponsored by the National Science Foundation.

References

Austin, J., N. Butchart, and K. P. Shine (1992), Possibility of an Arctic ozone hole in a doubled-CO_2 climate, *Nature*, *360*, 221–225.

Baldwin, M. P., and D. O'Sullivan (1995), Stratospheric effects of ENSO-related tropospheric circulation anomalies, *J. Clim.*, *8*, 649–667.

Blackmon, M. L., J. E. Geisler, and E. J. Pitcher (1983), A general circulation model study of January climate anomaly patterns associated with interannual variation of equatorial Pacific sea surface temperature, *J. Atmos. Sci.*, *40*, 1410–1425.

Brasseur, G. P., D. A. Hauglustaine, S. Walters, P. J. Rasch, J.-F. Müller, C. Granier, and X.-X. Tie (1998), MOZART, a global chemical transport model for ozone and related chemical tracers: 1. Model description, *J. Geophys. Res.*, *103*, 28,265–28,289.

Charney, J. G., and P. G. Drazin (1961), Propagation of planetary-scale disturbances from the lower into the upper atmosphere, *J. Geophys. Res.*, *66*, 83–109.

Considine, D. B., A. R. Douglass, D. E. Kinnison, P. S. Connell, and D. A. Rotman (2000), A polar stratospheric cloud parameterization for the global modeling initiative three-dimensional model and its response to stratospheric aircraft, *J. Geophys. Res.*, *105*, 3955–3975.

Dunkerton, T. J. (1978), On the mean meridional mass motions of the stratosphere and mesosphere, *J. Atmos. Sci.*, *35*, 2325–2333.

Friedl, R. (Ed.) (1997), Atmospheric effects of subsonic aircraft: Interim assessment report of the advanced subsonic technology program, *NASA Ref. Publ., 1400*, 143 pp.

Garcia, R. R., and M. L. Salby (1987), Transient response to localized episodic heating in the tropics. part 2: Far-field behavior, *J. Atmos. Sci.*, *44*, 499–530.

Hack, J. J., J. T. Kiehl, and J. W. Hurrell (1998), The hydrological and thermodynamic characteristics of the NCAR CCM3, *J. Clim.*, *11*, 1179–1206.

Hamilton, K. (1993), An examination of observed Southern Oscillation effects in the Northern Hemisphere stratosphere, *J. Atmos. Sci.*, *50*, 3468–3473.

Hamilton, K. (1995), Interannual variability in the Northern Hemisphere winter middle atmosphere in control and perturbed experiments with the GFDL SKYHI general circulation model, *J. Atmos. Sci.*, *52*, 44–66.

Hauglustaine, D. A., G. P. Brasseur, S. Walters, P. J. Rasch, J.-F. Müller, L. K. Emmons, and M. A. Carroll (1998), MOZART, a global chemical transport model for ozone and related chemical tracers: 2. Model results and evaluation, *J. Geophys. Res.*, *103*, 28,291–28,335.

Holton, J. R. (1982), The role of gravity waves induced drag and diffusion on the momentum budget of the mesosphere, *J. Atmos. Sci.*, *40*, 2497–2507.

Holton, J. R. (1983), The influence of gravity wave breaking on the general circulation of the middle atmosphere, *J. Atmos. Sci.*, *40*, 2497–2507.

Holton, J. R., and C. Mass (1976), Stratospheric vacillation cycles, *J. Atmos. Sci.*, *33*, 2218–2225.

Horel, J. D., and J. M. Wallace (1981), Planetary-scale atmospheric phenomena associated with the Southern Oscillation, *Mon. Weather Rev.*, *109*, 813–829.

Horowitz, L. W., et al. (2003), A global simulation of tropospheric ozone and related tracers: Description and evaluation of MOZART, version 2, *J. Geophys. Res.*, *108*(D24), 4784, doi:10.1029/2002JD002853.

Hurrell, J. W., J. J. Hack, B. A. Boville, D. L. Williamson, and J. T. Kiehl (1998), The dynamical simulation of the NCAR Community Climate Model Version 3 (CCM3), *J. Clim.*, *11*, 1207–1236.

Kiehl, J. T., J. J. Hack, G. B. Bonan, B. A. Boville, D. L. Williamson, and P. J. Rasch (1998a), The National Center for Atmospheric Research Community Climate Model, CCM3, *J. Clim.*, *11*, 1131–1149.

Kiehl, J. T., J. J. Hack, and J. W. Hurrell (1998b), The energy budget of the NCAR Community Climate Model: CCM3, *J. Clim.*, *11*, 1151–1178.

Kistler, R., et al. (2001), The NCEP-NCAR 50-Year Reanalysis: Monthly means CD-ROM and documentation, *Bull. Am. Meteorol. Soc.*, *82*, 247–268.

Leovy, C. B., C.-R. Sun, M. H. Hitchmann, E. E. Remsberg, J. M. Russell III, L. L. Gordley, J. C. Gille, and L. V. Lyjak (1985), Transport of ozone in the middle atmosphere: Evidence for planetary wave breaking, *J. Atmos. Sci.*, *42*, 230–244.

Lübken, F.-J. (2001), No long-term change of the thermal structure in the mesosphere at high latitudes during summer, *Adv. Space Res.*, *28*, 947–953.

Matsuno, T. (1971), A dynamical model of the stratospheric sudden warmings, *J. Atmos. Sci.*, *28*, 1479–1494.

McLandress, C., G. C. Shepherd, B. H. Solheim, M. D. Burrage, P. B. Hays, and W. R. Skinner (1996), Combined mesosphere/thermosphere winds using WINDII and HRDII data from the Upper Atmosphere Research Satellite, *J. Geophys. Res.*, *101*, 10,441–10,453.

Pickering, K. E., Y. Wang, W.-K. Tao, C. Price, and J.-F. Müller (1998), Vertical distributions of lightning NO_x for use in regional and global chemical transport models, *J. Geophys. Res.*, *103*, 31,203–31,216.

Price, C., J. Penner, and M. Prather (1997), NO_x from lightning: 2. Constraints from the global atmospheric electric circuit, *J. Geophys. Res.*, *102*, 5943–5951.

Rasch, P. J., N. W. Mahowald, and B. E. Eaton (1997), Representations of transport, convection, and the hydrological cycle in chemical transport models: Implication for the modeling short-lived and soluble species, *J. Geophys. Res.*, *102*, 28,127–28,138.

Salby, M. L., and R. R. Garcia (1987), Transient response to localized episodic heating in the tropics. part I. Excitation and short-time near field behavior, *J. Atmos. Sci.*, *44*, 458–498.

Saravanan, R. (1998), Atmospheric low frequency variability and its relationship to midlatitude SST variability: Studies using the NCAR Climate System Model, *J. Clim.*, *11*, 1386–1404.

Sassi, F., R. R. Garcia, B. A. Boville, and H. Liu (2002), On temperature inversions and the mesospheric surf zone, *J. Geophys. Res.*, *107*(D19), 4380, doi:10.1029/2001JD001525.

Scott, R. K., and P. H. Haynes (1998), Interannual variability of the extratropical stratospheric circulation: The low-latitude flywhell, *Q. J. R. Meteorol. Soc.*, *124*, 2149–2173.

Shindell, D. T., D. Rind, and P. Lonergan (1998), Increased polar stratospheric ozone losses and delayed eventual recovery owing to increasing greenhouse-gas concentrations, *Nature*, *392*, 589–592.

Taguchi, M., T. Yamaga, and S. Yoden (2001), Internal variability of the troposphere-stratosphere coupled system simulated in a simple global circulation model, *J. Atmos. Sci.*, *58*, 3184–3203.

van Loon, H., and K. Labitzke (1987), The Southern Oscillation. part V: The anomalies in the lower stratosphere of the Northern Hemisphere and a comparison with the Quasi-Biennial Oscillation, *Mon. Weather Rev.*, *115*, 357–369.

Williamson, D. L. (1997), Climate simulations with a spectral, semi-Lagrangian model with linear grids, in *Numerical Methods in Atmospheric and Ocean Modelling: The André J. Robert Memorial Volume*, edited by C. Lin, R. Laprise, and H. Ritchie, pp. 279–292, Can. Meteorol. and Oceanogr. Soc., Ottawa.

Williamson, D. L., and J. G. Olson (1994), Climate simulations with a semi-Lagrangian version of the NCAR Community Climate Model, *Mon. Weather Rev.*, *122*, 1594–1610.

Yulaeva, E., and J. M. Wallace (1994), The signature of ENSO in global temperature and precipitation fields derived from the Microwave Sounding Unit, *J. Clim.*, *7*, 1719–1736.

B. A. Boville, R. R. Garcia, D. Kinnison, R. Roble, and F. Sassi, National Center for Atmospheric Research, P.O. Box 3000, Boulder, CO 80307, USA. (boville@ucar.edu; rgarcia@ncar.ucar.edu; dkin@acd.ucar.edu; roble@ncar.ucar.edu; sassi@ncar.ucar.edu)